Applied Surface Science 634 (2023) 157629

Contents lists available at ScienceDirect

Applied Surface Science

journal homepage: www.elsevier.com/locate/apsusc

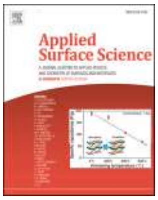

Full Length Article

Laser-synthesis of conductive carbon-based materials from two flexible commercial substrates: A comparison

Yann Houeix [a], Francisco J. Romero [a], Carmen L. Moraila [a], Almudena Rivadeneyra [a], Noel Rodriguez [a], Diego P. Morales [a], Alfonso Salinas-Castillo [b,*]

[a] *Dept. Electronics and Computer Technology, Faculty of Sciences, University of Granada, 18071 Granada, Spain*
[b] *Dept. Analytical Chemistry, Faculty of Sciences, University of Granada, 18071 Granada, Spain*

A R T I C L E I N F O

Keywords:
Laser ablation
Polyetherimide
Polyimide
Flexible electronics
Laser-induced graphene
Graphene-based materials
Carbon electrodes

A B S T R A C T

One of the key challenges in the field of flexible electronics relies on finding conductive materials that can withstand bending and stretching stresses while maintaining their performance. In this context, this work presents a comparative study of laser-induced conductive materials from the direct laser-scribing of two commercial flexible films: the benchmark Kapton® HN polyimide (PI) precursor and the Ultem^{TM} 1000 polyetherimide (PEI) alternative contender. The synthesis process on both materials is optimized in terms of electrical conductivity using a high-performance galvanometric laser with a wavelength of 532 nm for the fabrication of multiple samples at different laser powers and speeds. The samples are structurally characterized using Scanning Electron Microscopy (SEM), Raman spectroscopy, X-ray Photoelectron Spectroscopy (XPS), and Fourier-Transform Infrared Spectroscopy (FTIR) aiming at understanding the chemical and physical changes of the ablated material. The results demonstrate that the proposed setup is feasible for the synthesis of uniform and reliable conductive patterns on the surface of both substrates with high reproducibility. In particular, it is proved that PEI is more suitable precursor for flexible electronics applications which demand high electrical conductivity, leading to a sheet resistance of 3.62 ± 0.35 Ω/sq at 0.8 W and 5 mm/s once the laser-synthesis process is optimized (against the 6.04 ± 0.63 Ω/sq at 0.6 W and 5 mm/s offered by the LIG on PI). The performance of both laser-induced patterns as electrodes for the fabrication of electrochemical capacitors is also studied and compared in terms of areal specific capacitance.

1. Introduction

Carbon-derived nanomaterials including graphene and its counterparts have become a field of exponentially increasing investigation during the last fifteen years [1]. Their enormous interest is entailed by the myriad of applications in different areas of science and technology that can be conceived to outperform traditional materials in the fields of chemistry, healthcare, or energy storage. Among these, their use in the field of flexible electronics stands out due to their easy and inexpensive manufacturing process when compared with traditional flexible electronics materials as well as their unique electrical properties, and the possibility to create physical and chemical sensors with high sensitivity and fast response. Some examples are temperature sensors [2], gas sensors [3] or biosensors [4], and other kinds of devices such as diodes [5], solar cells [6], or capacitors [7]. Because of all these advantages, these kinds of materials are expected to play a key role in the future of the Internet of Things (IoT) [8].

Graphene has typically been suited as the best carbon-derived nanomaterial candidate for the majority of IoT applications, however, fabricating sheets capable of matching its theoretical properties have impeded their use in end-user applications. The different top-down or bottom-up approaches for the fabrication of high-quality graphene, such as epitaxial growth on Silicon Carbide or Chemical Vapor Deposition (CVD), require high-end and expensive technological instruments and lots of fabrication steps that increase the price and the difficulty of the mass production of samples. Therefore, these approaches are not in alignment with the idea of the ubiquity and cost-effectiveness required by the IoT paradigm. This has led to an emerging line of alternative solutions based on the use of lower crystallographic quality graphene-based materials instead, such as graphene oxide [9,10], graphene polymer composites [11,12], or Laser-Induced Graphene (LIG) [13,14] to get comparable electrical or mechanical properties as graphene, with

---

* Corresponding author.
E-mail address: alfonsos@ugr.es (A. Salinas-Castillo).

https://doi.org/10.1016/j.apsusc.2023.157629
Received 22 March 2023; Received in revised form 13 May 2023; Accepted 26 May 2023

much simpler and cheaper fabrication processes that do not require heavy chemicals or high energy consumption. Therefore, they contribute to a more sustainable electronics equipment lifecycle, from their production to their disposal, thus reducing both the environmental impact and the electronic waste (e-waste) when compared with traditional metal-based electronics [15].

In particular, in recent years LIG has been proposed as the best candidate for the fabrication of a wide range of eco-friendly devices thanks to its mask-less, chemicals-free and one-step fabrication process under ambient conditions. This technique constitutes a top-down production approach for the creation of electrically conductive and mechanically flexible patterns with a high surface area on top of different carbon-rich substrates [16,17]. The most important prerequisite for LIG production is that the precursor contains aromatic, imide or aliphatic repeating units, which are rearranged by the photoablation to form a graphitic structure [18,19]. Actually, it has been stipulated that any carbon source could be potentially a LIG precursor [20]. For instance, Claro et al. [19] exposed the production of green LIG (gLIG) from various renewable and sustainable carbon sources, such as cork [21], wood [22], or paper [23] for multiples applications, such as energy-storage devices or sensors [24–26].

Alternatively, LIG synthesized from Kapton® HN polyimide has also been found to be useful in a variety of applications, including supercapacitors [27], strain sensors [28], gas sensors [29] and liquid sensors [30] offering enhanced performance than other sustainable carbon sources. In fact, the laser scribing of flexible polymers has been used not only for the manufacturing of LIG patterns or fibers, but also for microfluidic channels and multilevel imprinting molds at once [31].

Furthermore, other kinds of polymers, not so known, could also be promising substrates for graphene precursors, such as polyetherimide (PEI) [32], polyetherketone (PEEK) [33], or polysulfone (PSU) [34]. Among them, PEI stands out by its excellent mechanical and thermal properties [35]. It was first developed in 1982 by Sabic as ULTEM® resin and is commonly used for 3D printing and in the automotive and aerospace industries. The synthesis of LIG on PEI has already been reported in the literature for supercapacitive applications [36] and tensile sensors [37]. The greater number of aromatic groups on the polymeric chain of the polyetherimide compared to the polyimide could lead to a greater graphitization of the polymer, as there are more groups likely to be ablated by laser irradiation. However, the quality and properties of the laser-synthetized materials are closely associated with the mechanism of laser reduction, and therefore, it is of high importance to study their synthesis under different conditions in order to tune and optimize the properties of the LIG on the different substrates to be used in end-user applications. The selection of both PI and PEI for their study as precursors for their conversion into conductive carbon-based materials by laser patterning at ambient conditions is based on their high glass transition and melting temperatures (T_g and T_m) [20]. Another important aspect is that both of them have demonstrated recyclability and reusability [38,39].

In this context, this work presents a comprehensive comparison of the laser ablation of both PI and PEI commercial films using a 532 nm wavelength laser. The laser-induced materials are then electrically characterized for different laser conditions (power and scanning speed) seeking the optimization of their electrical conductivity. For both substrates, the surface morphology is studied by means of Scanning Electron Microscopy (SEM), and the structural analysis is performed by Raman spectroscopy to validate the formation of a graphene-derived material, as well as both by X-ray Photoelectron Spectroscopy (XPS) and Fourier-Transform Infrared Spectroscopy (FTIR) to study the transformation of both polymers. The different characterization techniques were used to determine the optimal laser parameters for achieving the lowest resistivity in the resulting material without compromising the integrity of the substrate. Finally, once we optimized the overall laser synthesis process on both substrates, their electrochemical performance as electrodes for the fabrication of energy storage devices is also studied and compared in terms of specific capacitance.

2. Materials and methods

2.1. Materials

Two of the most common carbon-rich commercial polymers were used in this work as raw flexible substrates: ULTEM^{TM} 1000 Polyetherimide (PEI) films with a thickness of 200 µm from Prima Filaments®’ and Kapton® polyimide (PI) with a thickness of 150 µm from Guangyi Electronic Technology Co. On the one hand, PEI is made from a polycondensation reaction between bisphenol-A duanghdirte and diamene resulting in an amorphous engineering thermoplastic with high-temperature resistance and tensile strength [40]. On the other hand, Kapton® is produced by condensation of pyromellitic dianhydride and 4,4′-oxydianiline getting a stable polymer that is a good thermal and electrical insulator for a wide range of temperatures [41]. Before the laser scribing process, the surface of both materials was cleaned with isopropyl alcohol and, after drying for two minutes, the material was directly scribed at ambient conditions.

2.2. Laser scribing process

The laser scribing process was performed using a PowerLine E-12–532 Laser by Coherent® (Munich, Germany). This setup is a galvanometric pulsed laser with a wavelength of 532 nm (green light) with a maximal optical power of 6 W. The absorption properties of both precursor materials, measured with HP 8453 optical UV–Vis spectrometer equipment from Agilent Technologies (Santa Clara, CA, USA), demonstrated that they share a similar absorption coefficient for the 532 nm wavelength.

The system can scribe on a surface of 12 × 12 cm with a minimal focal point of about 50 µm. The parameters studied for tuning purposes are the optical output power of the laser and the speed of the beam. Moreover, the focal distance of the laser is 270 mm so the samples were placed at this distance to avoid the geometrical deformation of the engraved designs. The pulse frequency is set to its maximum value (50 kHz) to improve the scribing homogeneity and minimize the power required to achieve the ablation. The gap between two laser passes is set to 50 µm to, on the one hand, assure that two laser paths will be superposed obtaining a homogenous photoablation (thus avoiding unablated areas, as reported by other kinds of lasers [42]), and on the other hand, to minimize the scribing time.

A preliminary study was conducted to determine the optimal range of laser power and speed for achieving a low sheet resistance (<150 Ohm/sq.) and homogeneous samples without damaging the substrate. On this basis, the laser power was varied from 0.5 W to 1 W and the scan speed was modified from 5 to 60 mm/s. A fume extractor was located near the sample under treatment to remove the smoke generated as well as to avoid partial absorption of the irradiation energy by the exhausted particles. The designs were made by Visual Laser Studio, the proprietary software from Coherent®. To complete the pattern design, the laser

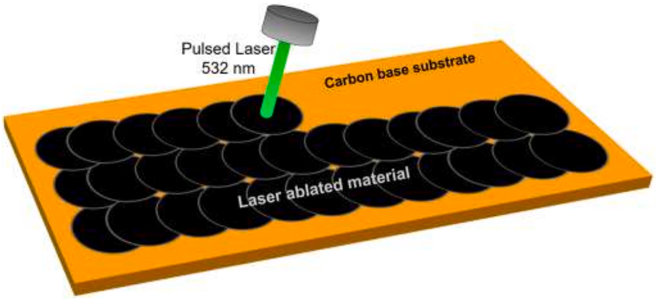

Fig. 1. Schematic diagram of the laser photoablation process.

performs horizontal superposed lines composed of multiple pulses, as schematized in Fig. 1. Rectangular samples of both materials were made for their characterization with a size of 12 × 7 mm. We fabricated a total of four batches for each substrate. A stabilization step is performed before the direct laser writing process, where the laser should be operating for at least 30 min at 0.75 W to achieve a stable point of operation, thus minimizing the variability from batch to batch.

2.3. Structural characterization

The microstructure of the samples irradiated by the laser was analyzed using the Scanning Electron Microscope (SEM) NVision40 from Carl Zeiss® (Oberkochen, Germany) at an extraction and acceleration voltage of 5 kV, otherwise noted.

A dispersive micro-Raman spectrometer JASCO NRS-5100 (Easton, PA, USA) with a green diode (Elforlight G4-30; Nd:YAG, l = 532 nm) as excitation source was used for the Raman spectra acquisition. The sampling parameters were: 10 accumulations with 3 s of exposure time.

The X-ray Photoelectron Spectroscopy (XPS) was carried out on a Kratos Axis Ultra-DLD (Manchester, UK), using an X-ray (Al Kα, $h\nu$ = 1486.6 eV) power of 450 W in a vacuum chamber where the pressure was kept below 10^{-10} Torr.

Fourier-transform infrared spectroscopy (FTIR) was performed by JASCO 6200 (Easton, PA, USA) and the spectra were analyzed with SPECTRA MANAGER v2 software. Optical images to get the sample thicknesses were acquired using a MOTICAM 5 + MP microscope-mounted camera.

2.4. Electrical characterization

Keysight® B2902A Source Meter Unit (Santa Rosa, California, USA) (SMU) was used to measure voltage and current for the electrical characterization of the produced patterns.

The method to evaluate the sheet resistance was the In-Line Four-Point Probe with the Dual-Configuration using the universal four-probe station from Jandel® (Eggington, UK) with a spacing between needles of 1 mm. This method allows for the elimination of contact and wire resistance, and it considers the non-idealities due to the sample size, performing high-precision sheet resistance measurements [43].

Each configuration of laser power/speed for every single batch was measured 40 times at ambient conditions. The value of sheet resistance was calculated as the mean value of all measurements and batches.

2.5. Electrochemical characterization

The InterDigital Electrodes (IDE) structure for electrochemical analysis was designed with the following specifications: the structure consisted of 20 fingers with 1 mm of interspacing between fingers and electrodes, resulting in a total effective area of around 4 cm^2. The IDEs were directly scribed on both substrates, while the electrical contact on each electrode was made using silver conductive lacquer (from RS PRO, Corby, Northants, UK, Product Number: 186–3600). The gel electrolyte was prepared by dissolving 1 g of poly(vinylalcohol) (PVA, from Sigma-Aldrich, St. Louis, MO, USA, Product Number: P1763) in 10 mL of deionized water (10 wt%) with stirring at 80 °C for 2 h using the MSH 140 magnetic stirrer (from Boeckel + Co, Hamburg, Germany). Once the PVA was completely dissolved, 1.5 mL of phosphoric acid (H_3PO_4, also from Sigma-Aldrich, product name: 1005731000) was added to the solution and it was stirred again for one hour [44–46]. Next, 2 mL of the resulting (PVA)/H_3PO_4 gel electrolyte was drop-casted on top of the IDE structure covering the effective area, as shown in Fig. 2. Cyclic Voltammetry (CV) measurements were carried out using a B2912A precision source-measurement unit (SMU) from Keysight Technologies, Inc. (St. Rose, CA, USA) with a potential window of ΔV = 1 V at various scanning rates. Finally, the areal specific capacitance as a function of the scan rate was extracted by Eq. (1) [47]:

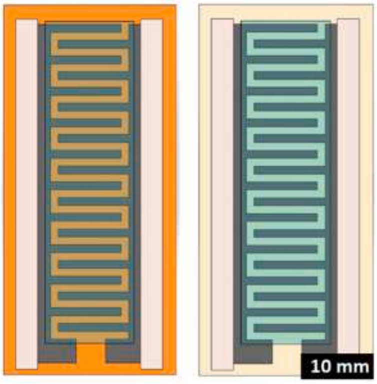

Fig. 2. Schematic representation of the fabricated electrochemical capacitors on both Kapton® HN (left) and ULTEM^{TM} 1000 PEI substrates (blue shadow color has been selected to make the electrolyte visible). (For interpretation of the references to color in this figure legend, the reader is referred to the web version of this article.)

$$C_A = \frac{1}{2\cdot A\cdot \Delta V\cdot s}\cdot\left(\int I(V)dV\right) \quad (1)$$

being A the area, ΔV the potential window, s the scan rate, and $I(V)$ the current response as a function of the voltage.

3. Results and discussion

3.1. Sheet resistance optimization

The resulting synthetized materials for different optical laser powers and scanning speeds are shown in Fig. 3 for both PI (left) and PEI (right) substrates. The laser power was ranged from 0.5 W to 1 W in steps of 0.1 W, whereas the scanning speeds was set from 5 mm/s to 60 mm/s, resulting in the laser power/speed pattern included in Fig. 3. We avoid the irradiation of the surface with the highest laser fluences (right upper corner), i.e., high power and low speed, to prevent damage to the substrate (as observed in the case of 0.7 W and 5 mm/s for the PI substrate). We can clearly observe different behaviors as a function of the laser power and speed for the different materials. In the case of the PI substrate, for high speeds and low laser powers (<0.01 J/mm) the laser fluence on the substrate is below the ablation threshold, i.e., it is not enough to induce a proper conversion of the PI into LIG. As the ratio power/speed increases, the resulting surfaces start showing a more uniform LIG layer without compromising the integrity of the substrate (range 0.01–0.02 J/mm). At this point, the thickness and the conductivity of the LIG are closely related to the laser fluence, as it is demonstrated later on. Increasing the ratio power/speed beyond that limit leads to the appearance of imperfections in the LIG layer, which make it easily detachable from the surface in the form of thin black fibers [48].

In the case of PEI, it is required a higher power/speed ratio (>0.025 J/mm) to induce the conductive patterns on its surface, since lower ratios are not enough to trigger the ablation process. Above this range, the conductive layer is present as a homogeneous and glassy pattern on top of the PEI. As in the case of PI, the electrical conductivity of these patterns also presents a high dependence with respect to the laser fluence, as shown in Fig. 4a and b at the different power levels and scan speeds.

The sheet resistance can be minimized by reaching a compromise between the laser power/speed and the capacity of the substrate to withstand the resulting laser fluence since, until the degradation of the substrate, the higher the ratio power/speed is, the lower the sheet resistance becomes (see Fig. 5). As seen, the transition from the raw material to a more electrically conductive state is more gradual in the case of PI [49], since the sheet resistance in the case of PEI exhibits an

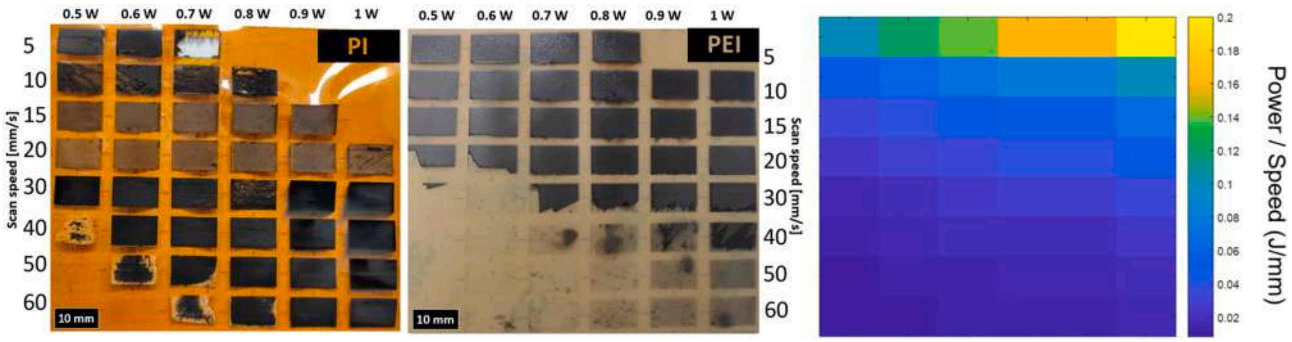

Fig. 3. Real images of fabricated samples at various laser power and scan speed conditions: on the right PEI and on the left PI.

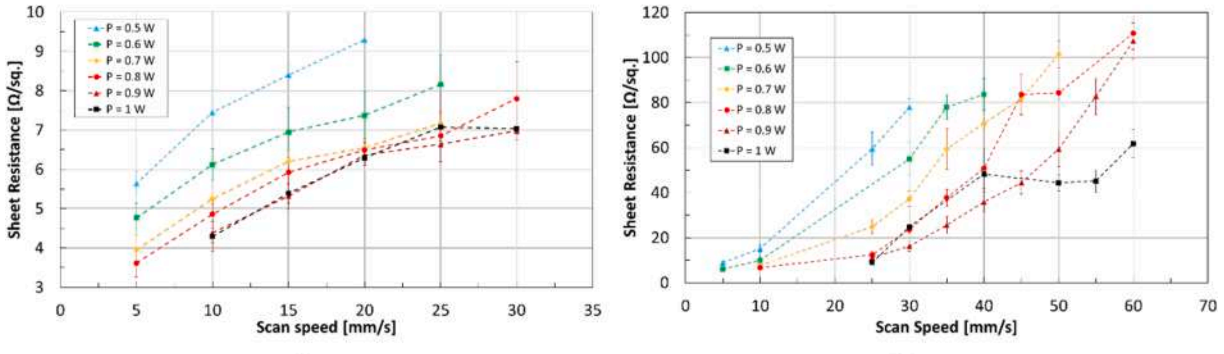

(a) (b)

Fig. 4. Sheet resistance as a function of laser power and scan speed conditions: (a) PEI (b) PI.

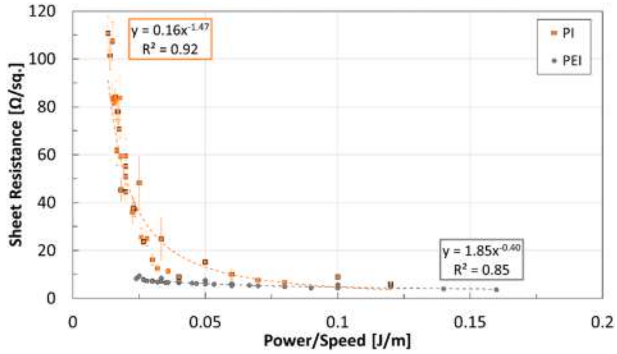

Fig. 5. Sheet Resistance in function of Power/Speed for PI in orange and PEI in grey. (For interpretation of the references to color in this figure legend, the reader is referred to the web version of this article.)

abrupt threshold once the ablation has occurred. In both cases, the conductivity of both materials presents an exponential dependency with respect to the ratio power/speed, obtaining the lowest sheet resistance of 3.62 ± 0.35 Ω/sq. for PEI (at 0.8 W and 5 mm/s) and 6.04 ± 0.63 Ω/sq. for PI (at 0.6 W and 5 mm/s), respectively. The variability of the sheet resistance is primarily due to the variability from batch to batch (being negligible the variability for the same sample).

In both cases, the results are promising when compared with other previous works reported in the literature, as reported in Table 1.

Nevertheless, a comprehensive comparison of the electrical conductivity of both materials requires removing the dependence with the thickness. For that, we can draw on the relationship between conductivity (σ), sheet resistance (R_{sh}) and thickness (t), which is given by [52]:

Table 1
Comparison of sheet resistance from laser-ablated PI and PEI substrate in recent studies.

Material	Laser	Sheet Resistance [Ω/sq.]	Ref.
PI	UV @ 355 nm	160	[50]
	UV @ 405 nm	250	[42]
		85	[51]
	CO_2 @ 10.6 µm	43	[27]
		20	[50]
		15	[18]
	Visible @ 532 nm	6.0	This work
PEI (ULTEM 9085)	CO_2 @ 10.6 µm	16	[36]
PEI (ULT-0090-E)		1.8	[37]
PEI (ULTEM 1000)	Visible @ 532 nm	3.6	This work

$$\sigma = \frac{1}{R_{sh} \cdot t} \tag{2}$$

On this basis, we obtained that the LIG on PEI presents a conductivity of 1821.8 S/m (for 0.8 W and 10 mm/s) with a film thickness of 118.6 µm, in contrast to the 1202.9 S/m (0.5 W and 5 mm/s) offered by the LIG layer of 93.07 µm on PI. We did not notice neither aging nor photoconductive effects in any of the laser-synthesized samples at ambient conditions, in contrast to other laser-reduced materials, such as reduced graphene oxide [53], which can experience modifications in their level of reduction due to different ambient conditions.

3.2. *Scanning electron microscope images*

SEM images of PEI samples are depicted in Fig. 6. In particular, Fig. 6a shows a top-view of the boundary between the raw PEI surface (on the right) and the porous surface of the induced material as a result of the laser photothermal process [18]. In Fig. 6b-c we can identify the

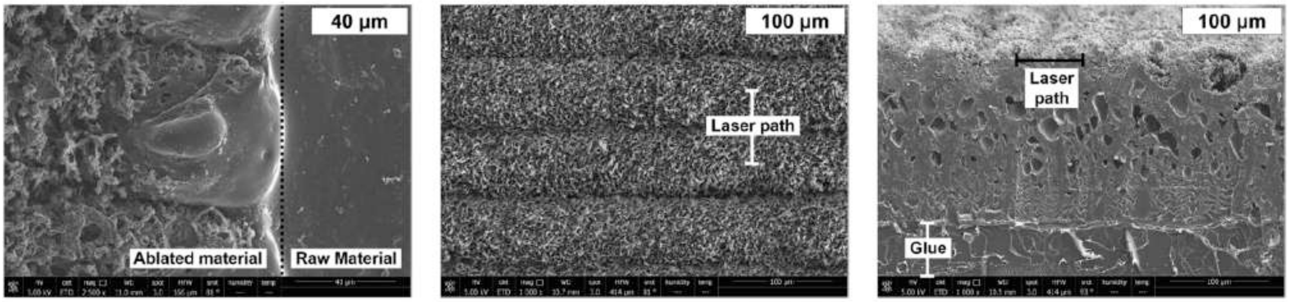

(a) (b) (c)

Fig. 6. SEM images at different magnifications of PEI ablated material at 0.8 W and 15 mm/s: (a) view of the limit between the ablated and raw surface. (b) overview of the ablated material and the laser paths. (c) cross-section of the sample.

foam-like nature of this material, which grows up homogeneously on top of the surface. We can also appreciate how the upper surface in this case presents a slight rippling as a consequence of the effect of the laser fluence on the effective diameter of the laser spot. Furthermore, although the upper surface of the LIG presents certain roughness, the cross-section of Fig. 6c reveals that the induced material counts with a thick cross-sectional area.

Similarly, Fig. 7 depicts the results obtained for the PI polyimide. In this case, the laser paths on the surface of the polyimide are not so easily identified as a consequence of the overlapping of the laser-induced patterns, which produces an overall layer formed by horizontal trenches, as shown in Fig. 7a. In addition, the cross-section of the material obtained on PI shows that it is much more porous than the obtained for PEI (Fig. 7c). In fact, the superior conductivity of LIG on PEI over PI can be attributed to its more uniform surface, lower porosity and less fragmented structure, which results in a higher cross-sectional area, thus decreasing the resistivity. The higher porosity and foam-like surface morphology of LIG make it more easily removable from the PI surface than the soft melty material synthetized on PEI. As seen on cross-section images, ablated PI seems much easier to peel off, being readily identifiable the limit between the LIG and the substrate. To avoid this, using a protective coating for the laser-induced materials is a common approach that can be found in the literature [54].

3.3. Raman spectroscopy

Raman spectra were obtained to understand the crystallography and the quality of the material induced on the substrate surface by laser irradiation. Fig. 8a and b show the Raman spectra of the material induced on PEI and PI, respectively. As seen, we can identify the three main Raman peaks which are associated with carbon-based materials: D, G, and 2-nd order D (2D) peaks [55]. The G and D peaks are present at 1580 and 1350 cm^{-1}, respectively, in both materials. The first one indicates the planar configuration sp^2 bonded carbon that constitutes these two graphitic-based materials, while the D peak reveals the presence of defects in this latter structure [56,57]. Second order D-band (2D - sometimes referred to as G'-band) located at ~2700 cm^{-1} can also be identified for some of the patterns induced on the substrates. It is known that the crystallographic quality of the material is directly related to the I_G/I_D ratio and that the I_{2D} intensity and width at half-maximum (FWHM$_{2D}$) can be associated with graphene-based materials and high-ordered pyrolytic graphite (HOPG) [58]. For instance, the Raman spectrum of pristine graphene is characterized by the absence of the D peak, given its perfectly ordered honeycomb structure, as well as by an intensity ratio I_{2D}/I_G of 2–3 indicating its monolayer nature (this ratio decreases as the number of graphene layer increases) [17,59].

Therefore, based on the Raman results, we concluded that the material synthesized on top of the PI substrate for a proper laser configuration (range 0.01–0.02 J/mm) can be identified as laser-induced graphene, a disordered and multi-layer graphene-based material with $I_G/I_D > 1$ and an appreciable 2D peak. However, in the case of the PEI substrate, the results are similar to those obtained when the PI is irradiated with a laser fluence well beyond the ablation threshold. In this case, the material obtained is identified as glassy and amorphous carbon [17].

3.4. XPS spectroscopy

The structure of the samples was also analyzed by XPS. Then, Fig. 9a and 9b show XPS surveys of both materials, proving that the substrates are mainly composed of carbon, oxygen and nitrogen, as expected. The initial concentrations of the main components for both raw substrates together with the theoretical values are given in Table 2.

The atomic quantifications presented in Table 2 for PEI and PI demonstrate that the laser-irradiation process implies an increase in the carbon concentration and a reduction of the oxygen-containing

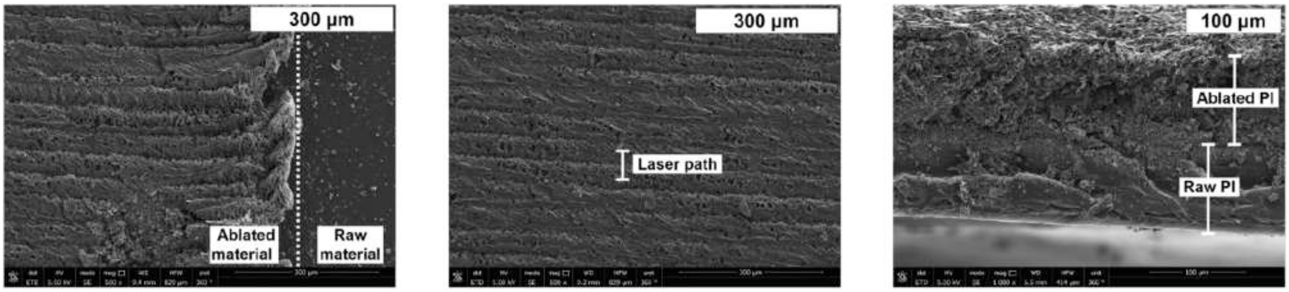

(a) (b) (c)

Fig. 7. SEM images at different magnifications of PI ablated material at 0.5 W and 5 mm/s: (a) view of the limit between the ablated and raw surface. (b) overview of the ablated material and the laser paths. (c) cross-section of the sample.

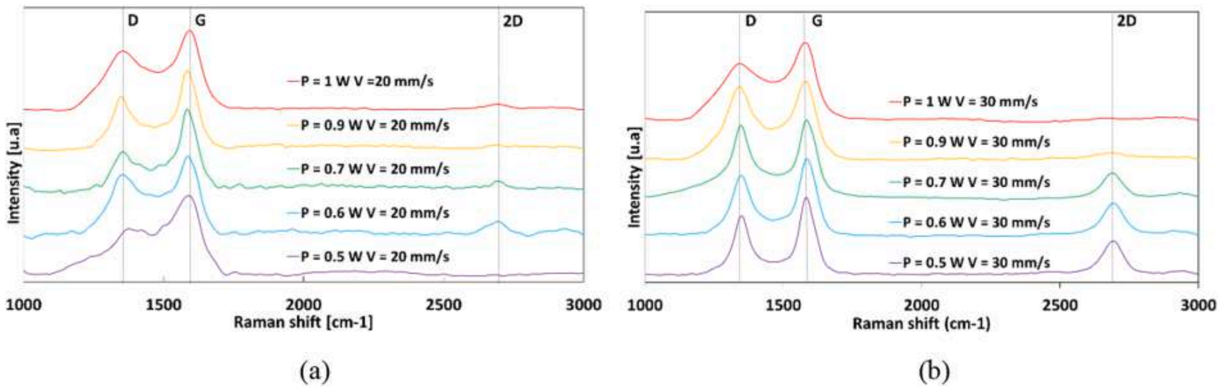

(a) (b)

Fig. 8. Raman spectrum of (a) PEI and (b) PI for different laser power.

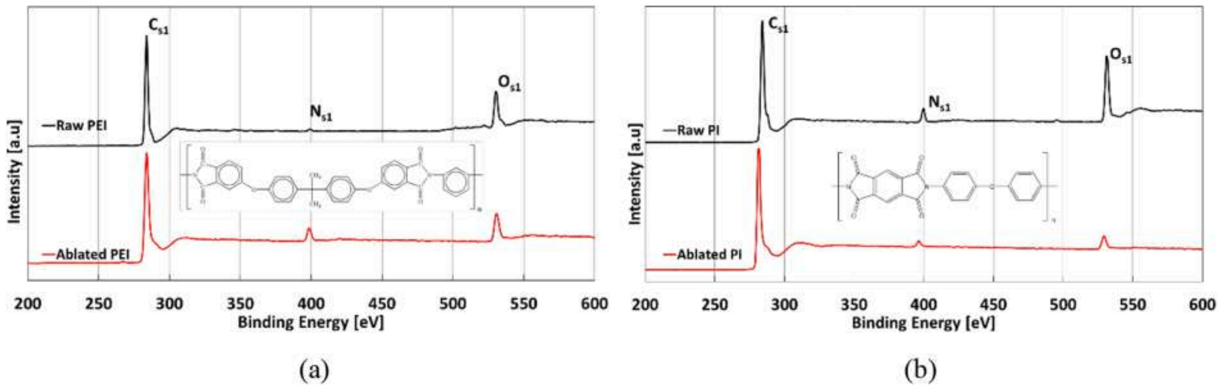

(a) (b)

Fig. 9. General XPS spectrum before (black) and after laser irradiation (red) of (a) PEI (laser ablation at 0.8 W, 20 mm/s) and (b) PI (laser ablation at 0.8 W, 40 mm/s) samples. (For interpretation of the references to color in this figure legend, the reader is referred to the web version of this article.)

Table 2
Atomic concentration of PEI and PI samples for different laser power at a scanning speed of 20 mm/s.

PEI	C_{s1}	O_{s1}	N_{s1}	C/O	PI	C_{s1}	O_{s1}	N_{s1}	C/O
Theory	82.22	13.33	0.04	6.17	Theory	75.86	17.24	6.90	4.40
Raw	81.24	12.36	1.05	6.57	Raw	78.26	15.52	4.38	5.04
0.6 W	84.33	9.88	5.79	8.54	0.6 W	94.77	3.20	2.03	29.61
0.8 W	84.50	11.01	4.49	7.68	0.8 W	93.55	3.78	2.67	24.70
1 W	86.38	10.13	3.49	8.52	1 W	93.36	3.97	2.67	23.52

functional groups. This fact is a consequence of the photothermal effect induced by the laser, producing an increase of the material temperature and the vibration of the atomic lattice easily breaking the different C—O, C═O bonds which are recombined and released in form of gases (O_2, CO_2, etc.) [60,61]. Despite this, we can identify clear differences in the laser photothermal results for each substrate. On one hand, note that the concentration of nitrogen increases after the laser irradiation for PEI, indicating that the reaction taking place involves the addition of

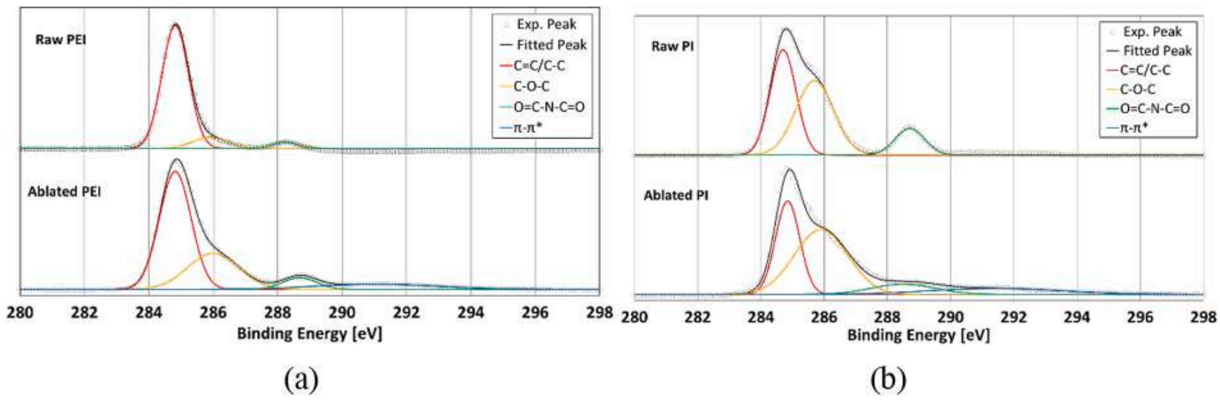

(a) (b)

Fig. 10. Comparison of C_{s1} deconvolution peaks from XPS spectrum of (a) PEI samples and (b) PI samples before and after laser irradiation.

nitrogen from the air. Therefore, the N_2 molecules from the air are ionized during the high photon energy irradiation, and the ionized nitrogen reacts with the polymer forming new nitrogen-containing groups on the surface of the material [62]. This effect is more noticeable for low laser fluences since as the laser power increases the larger number of CNC bonds that are broken compensates this effect. On the other hand, we can also observe that the increase of the C/O ratio is much higher in the case of the PI substrate. This indicates that the laser-photothermal process produces a recombination of the oxygen-containing functional groups of the PEI, thus leading to a more conductive state; while in the case of PI these bonds are completely broken, which explains that the laser irradiation on PI produces much more gases than on PEI.

When analyzing the C_{s1} peaks before and after the laser irradiation (Fig. 10), we can identify the contribution of both single and double carbon bonds (C—C, C═C) at 284.8 eV, together with the ether (C—O—C, 286 eV) and imide (O—C—N—C—O, 288.3 eV) bonds which compose the PEI and PI structure [63–66]. Here we can also appreciate that, after the laser irradiation on the PEI samples, there is no significant decrease in the oxygen and the nitrogen atomic percentages with respect to the raw material, as occurs in the case of the LIG obtained from PI. As seen in Fig. 10a, there is still a high contribution of ether and imide compounds in the ablated PEI C_{s1} peak. However, it is also appreciable the emergence of π-π^* transition on both ablated polymers, which is a characteristic shake-up line (satellite peak) for carbon in aromatic compounds. Since the π bond is a characteristic feature of sp^2 hybridization, it supports that the laser ablation produces a rearrangement of the aromatic compounds with a higher prevalence of sp^2 components, which also explains the increase of the electrical conductivity [67–69].

3.5. *FTIR spectroscopy*

FTIR is a useful tool to infer the chemical and molecular structure of carbon-based materials. Fig. 11a-b show the FTIR transmittance spectrum of raw samples, in black, and the modification of their structures after the laser ablation, in red. For both materials, related results are expected as both polymers have similar bonds, with more pronounced peaks on raw PEI due to the longer polymer chain. The non-treated samples contain features characteristic at 1775 and 1720 cm^{-1} (typical of imide carbonyl symmetric and asymmetric stretches), at 1355 cm^{-1} and 745 cm^{-1} (C—N stretching and bending), and at 1234 cm^{-1} (aromatic ether, C—O—C) [70,71 60]. The band at 1060 cm^{-1} is formed by the stretching CO (alkoxy) [72]. The aromatic group C—C is presented at 1600 and 1490 cm^{-1}, and finally the C—H group at 820 cm^{-1} [73].

The laser irradiation has decreased most of the peaks, in particular: aromatic C—H, imide C—N, and aromatic ether C—O—C. This variation indicates the reduction of oxygen functionalities and the synthesis of a reduced form of the original polymer. As seen in the previous result, the effect of the laser ablation is more present in PI, getting flatter peaks than in PEI substrate after the laser treatment.

3.6. *Electrochemical analysis*

In the previous sections, we have analyzed the material synthesized from an electrical and structural point of view. The results demonstrate that although both materials count with notable differences in their structure, they present a similar electrical conductivity. However, there are different parameters of interest apart from the electrical conductivity when developing flexible electronic devices. Since the conductive patterns on PEI are more conductive, they could be considered the preferred ones for different types for this purpose. However, other properties, such as the porosity of the resulting material can also be of high interest for other kinds of applications involving, e.g., catalysis or electrochemical reactions. In this context, here we compare both PEI and PI precursors for the fabrication of flexible electrochemical capacitors. Therefore, the laser-photothermal process has been used to fabricate InterDigital Electrodes (IDE) directly on both substrates. Then, a Cyclic Voltammetry (CV) test is performed for the evaluation of the energy storage ability of the induced materials using $(PVA)/H_3PO_4$ as electrolyte.

The results obtained, plotted in Fig. 12, demonstrate that both configurations offer a pseudorectangular and highly symmetric shape over increasing scan rates, indicating a good reversible electric double-layer capacitor behavior. The specific areal capacitance, as expressed in Equation (1), is presented in Fig. 12b and d for PEI and PI, respectively. As seen, the higher porosity of the LIG on PI contributes to a larger specific areal capacitance (>100 times higher) thanks to a deeper electrolyte ions penetration into the material's pores [74]. In addition, this penetration of the ions is maintained even at high scan rates, as manifested by the almost flat response of the areal capacitance as the scan rates increase. On the contrary, for PEI, increasing the scan rate worsen the penetration depth of these ions even more, thus leading to a progressive depletion of the overall capacitance.

4. Conclusions

In this research, two commercial flexible materials have been used for the laser-induction of conductive carbon-based patterns at ambient conditions: Kapton® polyimide (PI) films and ULTEM^{TM} 1000 polyetherimide (PEI) sheets. The laser synthesis process was carried out using a galvanometric laser with a wavelength of 532 nm, comparing the results and optimizing the laser parameters with the goal of minimizing the resistivity of the induced patterns. The different samples were fabricated and electrically analyzed showing that the minimum sheet resistance occurs at the maximum energy density before combustion of the substrate, obtaining homogeneous and stable sheet resistances that can be optimized to achieve values as low as 3.62 ± 0.35 Ω/sq. for PEI

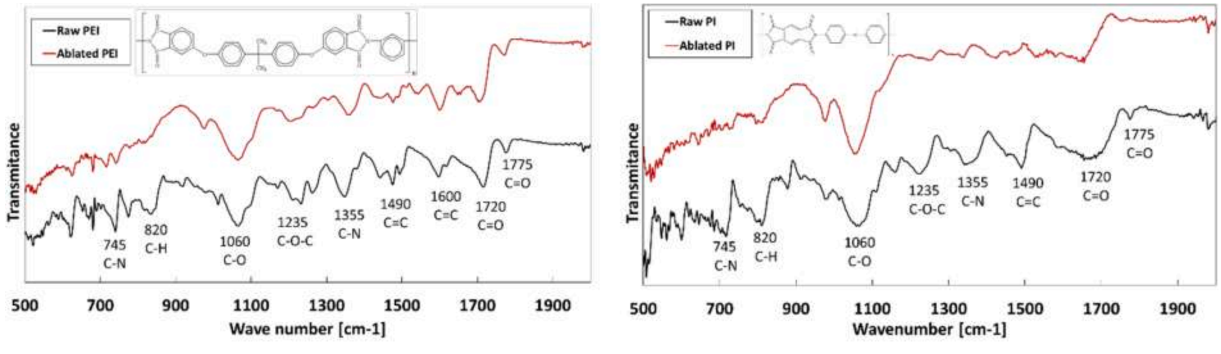

(a) (b)

Fig. 11. FTIR spectrum before (black) and after laser irradiation (red) of (a) PEI and (b) PI samples. (For interpretation of the references to color in this figure legend, the reader is referred to the web version of this article.)

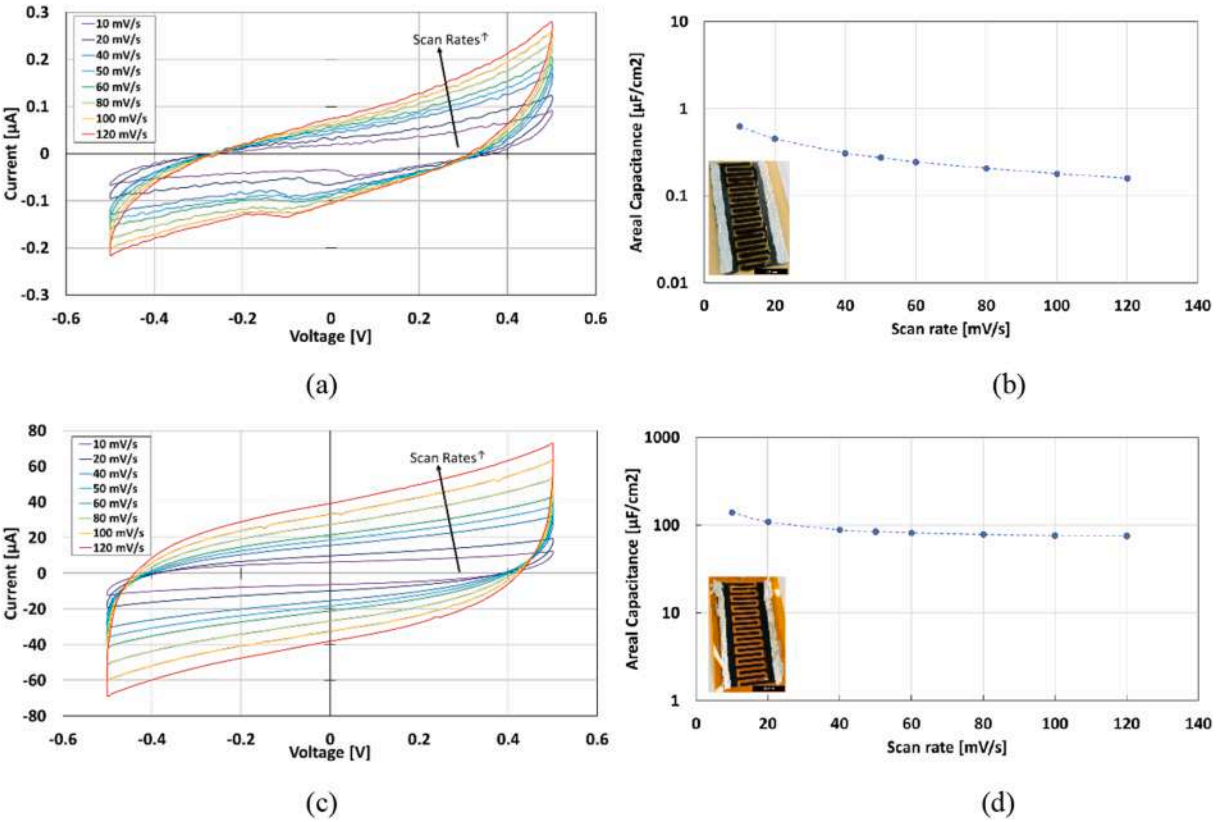

(a) (b)

(c) (d)

Fig. 12. Electrochemical behavior of IDE capacitor at scan rates of 10, 20, 40, 60, 80, 100, 120 mV/s. Cyclic voltametric curves for PEI (a) and PI (c). Computed areal capacitance (C_A) for PEI (b) and PI (d).

and 6.04 ± 0.63 Ω/sq. PI, where the error is mainly due to the variability from batch to batch. The resulting material on both substrates was morphologically, structurally, and chemically analyzed and compared through SEM, Raman, XPS and FTIR spectroscopy. The results show that, while the material obtained from the laser irradiation of the PI corresponds with laser-induced graphene (LIG, also known as porous graphene), in the case of PEI the material synthesized corresponds to glassy carbon, an amorphous conductive material. The less-porous structure of the glassy carbon makes this material more conductive than the LIG, although after a proper optimization of the laser parameters we can obtain comparable resistivities. However, the higher capacity of modulating the resistance of the LIG, as well as its porosity can also be highly interesting for certain kinds of applications. In this context, we have also demonstrated the superiority of LIG over glassy carbon derived from PEI for its application for the development of electrodes for energy storage applications.

CRediT authorship contribution statement

Yann Houeix: Investigation, Methodology, Validation, Writing – original draft. **Francisco J. Romero:** Investigation, Conceptualization, Formal analysis, Validation, Writing – original draft, Funding acquisition. **Carmen L. Moraila:** Investigation, Methodology, Validation, Writing – review & editing. **Almudena Rivadeneyra:** Investigation, Conceptualization, Methodology, Writing – review & editing, Funding acquisition. **Noel Rodriguez:** Supervision, Resources, Writing – review & editing, Project administration. **Diego P. Morales:** Resources, Supervision, Funding acquisition. **Alfonso Salinas-Castillo:** Supervision, Resources, Writing – review & editing, Project administration.

Declaration of Competing Interest

The authors declare that they have no known competing financial interests or personal relationships that could have appeared to influence the work reported in this paper.

Data availability

Data will be made available on request.

Acknowledgments

This work was supported by the FEDER/Junta de Andalucía-Consejería de Transformación Económica, Industria, Conocimiento y Universidades Project P20_00265 and Project BRNM-680-UGR20; Project TED2021-129949A-I00 funded by MCIN/AEI/10.13039/501100011033 and by European Union NextGenerationEU/PRTR; and Grant PID2020-117344RB-I00 funded by MCIN/AEI 10.13039/501100011033. In addition, this work was also supported by the Junta de Andalucía – Consejería de Universidad, Investigación e Innovación through the project ProyExcel_00268 as well as by the Spanish Ministry of Sciences and Innovation through the Ramón y Cajal fellow RYC2019-027457-I, the María Zambrano fellow C21.I4.P1 and the pre-doctoral grant PRE2021-096886.

References

[1] L.-X. Dong, Q. Chen, Properties, synthesis, and characterization of graphene, Front. Mater. Sci. China 4 (2010) 45–51.

[2] B. Davaji, H.D. Cho, M. Malakoutian, J.-K. Lee, G. Panin, T.W. Kang, C.H. Lee, A patterned single layer graphene resistance temperature sensor, Sci. Rep. 7 (2017) 1–10.

[3] J. Wu, K. Tao, Y. Guo, Z. Li, X. Wang, Z. Luo, S. Feng, C. Du, D. Chen, J. Miao, others, A 3D chemically modified graphene hydrogel for fast, highly sensitive, and selective gas sensor, Adv. Sci. 4 (2017) 1600319.

[4] Q. He, S. Wu, Z. Yin, H. Zhang, Graphene-based electronic sensors, Chem. Sci. 3 (2012) 1764–1772.

[5] D. Dragoman, M. Dragoman, R. Plana, Graphene-based ultrafast diode, J. Appl. Phys. 108 (2010), 084316.

[6] M. Sang, J. Shin, K. Kim, K.J. Yu, Electronic and thermal properties of graphene and recent advances in graphene based electronics applications, Nanomaterials 9 (2019), https://doi.org/10.3390/nano9030374.

[7] S. Vivekchand, C.S. Rout, K. Subrahmanyam, A. Govindaraj, C.N.R. Rao, Graphene-based electrochemical supercapacitors, J. Chem. Sci. 120 (2008) 9–13.

[8] S. Eigler, A. Hirsch, Chemistry with graphene and graphene oxide—challenges for synthetic chemists, Angew. Chem. Int. Ed. 53 (2014) 7720–7738.

[9] D.R. Dreyer, S. Park, C.W. Bielawski, R.S. Ruoff, The chemistry of graphene oxide, Chem. Soc. Rev. 39 (2010) 228–240.

[10] V. Singh, D. Joung, L. Zhai, S. Das, S.I. Khondaker, S. Seal, Graphene based materials: past, present and future, Prog. Mater Sci. 56 (2011) 1178–1271.

[11] X. Huang, Z. Yin, S. Wu, X. Qi, Q. He, Q. Zhang, Q. Yan, F. Boey, H. Zhang, Graphene-based materials: synthesis, characterization, properties, and applications, Small 7 (2011) 1876–1902.

[12] M. Fang, K. Wang, H. Lu, Y. Yang, S. Nutt, Covalent polymer functionalization of graphene nanosheets and mechanical properties of composites, J. Mater. Chem. 19 (2009) 7098–7105.

[13] R. Ye, D.K. James, J.M. Tour, Laser-induced graphene: from discovery to translation, Adv. Mater. 31 (2019) 1803621.

[14] A. Kaidarova, J. Kosel, Physical sensors based on laser-induced graphene: a review, IEEE Sens. J. 21 (2020) 12426–12443.

[15] S. Nandy, E. Fortunato, R. Martins, Green economy and waste management: an inevitable plan for materials science, Prog. Nat. Sci.: Mater. Int. (2022).

[16] G. Li, Direct laser writing of graphene electrodes, J. Appl. Phys. 127 (2020), 010901.

[17] K. Muzyka, G. Xu, Laser-induced graphene in facts, numbers, and notes in view of electroanalytical applications: a review, Electroanalysis 34 (2022) 574–589.

[18] J. Lin, Z. Peng, Y. Liu, F. Ruiz-Zepeda, R. Ye, E.L. Samuel, M.J. Yacaman, B. I. Yakobson, J.M. Tour, Laser-induced porous graphene films from commercial polymers, Nat. Commun. 5 (2014) 1–8.

[19] P.I.C. Claro, T. Pinheiro, S.L. Silvestre, A.C. Marques, J. Coelho, J.M. Marconcini, E. Fortunato, L.H.C. Mattoso, R. Martins, Sustainable carbon sources for green laser-induced graphene: a perspective on fundamental principles, applications, and challenges, Appl. Phys. Rev. 9 (2022).

[20] Y. Chyan, R. Ye, Y. Li, S.P. Singh, C.J. Arnusch, J.M. Tour, Laser-induced graphene by multiple lasing: toward electronics on cloth, paper, and food, ACS Nano 12 (2018) 2176–2183.

[21] A. Imbrogno, J. Islam, C. Santillo, R. Castaldo, L. Sygellou, C. Larrigy, R. Murray, E. Vaughan, M.K. Hoque, A.J. Quinn, et al., Laser-Induced graphene supercapacitors by direct laser writing of cork natural substrates, ACS Appl. Electron. Mater.. 4 (2022) 1541–1551.

[22] R. Ye, Y. Chyan, J. Zhang, Y. Li, X. Han, C. Kittrell, J.M. Tour, Laser-induced graphene formation on wood, Adv. Mater. 29 (2017) 1702211.

[23] T. Pinheiro, R. Correia, M. Morais, J. Coelho, E. Fortunato, M.G.F. Sales, A. C. Marques, R. Martins, Water peel-off transfer of electronically enhanced, paper-based laser-induced graphene for wearable electronics, ACS Nano 16 (2022) 20633–20646.

[24] J. Coelho, R.F. Correia, S. Silvestre, T. Pinheiro, A.C. Marques, M.R.P. Correia, J. V. Pinto, E. Fortunato, R. Martins, based laser-induced graphene for sustainable and flexible microsupercapacitor applications, Microchim. Acta 190 (2023) 40.

[25] Y. Jung, J. Min, J. Choi, J. Bang, S. Jeong, K.R. Pyun, J. Ahn, Y. Cho, S. Hong, S. Hong, others, Smart paper electronics by laser-induced graphene for biodegradable real-time food spoilage monitoring, Appl. Mater. Today 29 (2022), 101589.

[26] B. Kulyk, B.F. Silva, A.F. Carvalho, S. Silvestre, A.J. Fernandes, R. Martins, E. Fortunato, F.M. Costa, Laser-induced graphene from paper for mechanical sensing, ACS Appl. Mater. Interfaces 13 (2021) 10210–10221.

[27] F.J. Romero, D. Gerardo, R. Romero, I. Ortiz-Gomez, A. Salinas-Castillo, C. L. Moraila-Martinez, N. Rodriguez, D.P. Morales, Comparison of laser-synthetized nanographene-based electrodes for flexible supercapacitors, Micromachines 11 (2020) 555.

[28] A.F. Carvalho, A.J. Fernandes, C. Leitão, J. Deuermeier, A.C. Marques, R. Martins, E. Fortunato, F.M. Costa, Laser-induced graphene strain sensors produced by ultraviolet irradiation of polyimide, Adv. Funct. Mater. 28 (2018) 1805271.

[29] M.G. Stanford, K. Yang, Y. Chyan, C. Kittrell, J.M. Tour, Laser-induced graphene for flexible and embeddable gas sensors, ACS Nano 13 (2019) 3474–3482.

[30] Y. Wang, Z. Niu, J. Chen, Y. Zhai, Y. Xu, S. Luo, Freestanding laser induced graphene paper based liquid sensors, Carbon 153 (2019) 472–480.

[31] J. Lim, S. Park, H. Cho, Y. Lee, I. Ha, Y. Kim, E. Hwang, H. Lee, J. Shin, J. Kwon, others, Monolithic digital patterning of polyimide by laser-induced pyrolytic jetting, Chem. Eng. J. 428 (2022), 131050.

[32] X. Dai, J. Wu, Z. Qian, H. Wang, J. Jian, Y. Cao, M.H. Rummeli, Q. Yi, H. Liu, G. Zou, Ultra-smooth glassy graphene thin films for flexible transparent circuits, Sci. Adv. 2 (2016) e1601574.

[33] A. Lamberti, M. Serrapede, G. Ferraro, M. Fontana, F. Perrucci, S. Bianco, A. Chiolerio, S. Bocchini, All-SPEEK flexible supercapacitor exploiting laser-induced graphenization, 2D Materials 4 (2017), 035012.

[34] S.P. Singh, Y. Li, J. Zhang, J.M. Tour, C.J. Arnusch, Sulfur-doped laser-induced porous graphene derived from polysulfone-class polymers and membranes, ACS Nano 12 (2018) 289–297.

[35] J. Belana, J. Canadas, J. Diego, M. Mudarra, R. Diaz, S. Friederichs, C. Jaimes, M. Sanchis, Physical ageing studies in polyetherimide ULTEM 1000, Polym. Int. 46 (1998) 29–32.

[36] L. Jiao, Z.Y. Chua, S.K. Moon, J. Song, G. Bi, H. Zheng, B. Lee, J. Koo, Laser-induced graphene on additive manufacturing parts, Nanomaterials 9 (2019) 90.

[37] M. Tavakkoli Gilavan, M.S. Rahman, A. Minhas-Khan, S. Nambi, G. Grau, One-Step fabrication of low-resistance conductors on 3D-Printed structures by laser-induced graphene, ACS Appl. Electron. Mater. 3 (2021) 3867–3875.

[38] L. Olifirov, S. Kaloshkin, K. Ergin, V. Tcherdyntsev, V. Danilov, Solid-state recycling of polyimide film waste, J. Appl. Polym. Sci. 127 (2013) 2960–2968.

[39] Y.-T. Hwang, S. Ahn, H.-I. Koh, J. Park, H.-S. Kim, Evaluation of mechanical/dynamic properties of polyetherimide recycled polymer concrete for reducing rail slab noise, Functional Compos. Struct. 1 (2019), 025002.

[40] Omnexus, Polyetherimide (PEI): A Comprehensive Review, (n.d.). https://omnexus.specialchem.com/selection-guide/polyetherimide-pei-high-heat-plastic (accessed March 11, 2023).

[41] R.G. Bryant, Polyimides, in: Ullmann's Encyclopedia of Industrial Chemistry, John Wiley & Sons, Ltd, 2014, pp. 1–27. https://doi.org/10.1002/14356007.a21_253.pub2.

[42] F.J. Romero, A. Salinas-Castillo, A. Rivadeneyra, A. Albrecht, A. Godoy, D. P. Morales, N. Rodriguez, In-depth study of laser diode ablation of kapton polyimide for flexible conductive substrates, Nanomaterials 8 (2018) 517.

[43] Standard Test Method for Sheet Resistance Uniformity Evaluation by In-Line Four-Point Probe with the Dual-Configuration Procedure, American Society for Testing and Materials. 10.04 (1997) 13. https://doi.org/10.1520/F1529-02.

[44] J.-Y. Shieh, S.-H. Zhang, C.-H. Wu, H.H. Yu, A facile method to prepare a high performance solid-state flexible paper-based supercapacitor, Appl. Surf. Sci. 313 (2014) 704–710.

[45] D. He, A.J. Marsden, Z. Li, R. Zhao, W. Xue, M.A. Bissett, Fabrication of a graphene-based paper-like electrode for flexible solid-state supercapacitor devices, J. Electrochem. Soc. 165 (2018) A3481.

[46] R. Singh, C.C. Tripathi, Electrochemical exfoliation of graphite into graphene for flexible supercapacitor application, Mater. Today: Proc. 5 (2018) 1125–1130.

[47] Y. Chen, X. Zhang, D. Zhang, P. Yu, Y. Ma, High performance supercapacitors based on reduced graphene oxide in aqueous and ionic liquid electrolytes, Carbon 49 (2011) 573–580.

[48] R. Murray, M. Burke, D. Iacopino, A.J. Quinn, Design of experiments and optimization of laser-induced graphene, ACS Omega 6 (2021) 16736–16743.

[49] D. Zeng, K.C. Yung, C. Xie, Near-threshold ultraviolet-laser ablation of Kapton film investigated by x-ray photoelectron spectroscopy, J. Mater. Res. 18 (2003) 53–59.

[50] L. Wang, Z. Wang, A.N. Bakhtiyari, H. Zheng, A comparative study of laser-induced graphene by CO_2 infrared laser and 355 nm ultraviolet (UV) laser, Micromachines 11 (2020) 1094.

[51] M. Burke, C. Larrigy, E. Vaughan, G. Paterakis, L. Sygellou, A.J. Quinn, G. Herzog, C. Galiotis, D. Iacopino, Fabrication and electrochemical properties of three-dimensional (3D) porous graphitic and graphenelike electrodes obtained by low-cost direct laser writing methods, ACS Omega 5 (2020) 1540–1548.

[52] L. Li, W.M. Au, T. Hua, K.S. Wong, Design of a conductive fabric network by the sheet resistance method, Text. Res. J. 81 (2011) 1568–1577.

[53] H. Liang, W. Ren, J. Su, C. Cai, Photoconductivity of reduced graphene oxide and graphene oxide composite films, Thin Solid Films 521 (2012) 163–167.

[54] M. Marengo, G. Marinaro, J. Kosel, Flexible temperature and flow sensor from laser-induced graphene, in: 2017 IEEE SENSORS, IEEE, 2017: pp. 1–3.

[55] L. Bokobza, J.-L. Bruneel, M. Couzi, Raman spectra of carbon-based materials (from graphite to carbon black) and of some silicone composites, C. 1 (2015) 77–94.

[56] D.S. Knight, W.B. White, Raman and fluorescence spectroscopic characterization of diamonds and CVD diamond films, in: Raman Scattering, Luminescence and Spectroscopic Instrumentation in Technology, SPIE, 1989: pp. 144–151.

[57] X. Gu, Raman spectroscopy and the effects of ultraviolet irradiation on polyimide film, Appl. Phys. Lett. 62 (1993) 1568–1570.

[58] A.F. Alba, J. Totoricaguena-Gorriño, L. Campos-Arias, N. Peřinka, L. Ruiz-Rubio, J. L. Vilas-Vilela, S. Lanceros-Méndez, F.J. del Campo, Laser-induced highly oriented pyrolytic graphite for high-performance screen-printed electrodes, Mater. Adv. 2 (2021) 5912–5921.

[59] J.-B. Wu, M.-L. Lin, X. Cong, H.-N. Liu, P.-H. Tan, Raman spectroscopy of graphene-based materials and its applications in related devices, Chem. Soc. Rev. 47 (2018) 1822–1873.

[60] H. Zheng, T. Tan, W. Zhou, Studies of KrF laser-induced long periodic structures on polyimide, Opt. Lasers Eng. 47 (2009) 180–185.

[61] M. Inagaki, S. Harada, T. Sato, T. Nakajima, Y. Horino, K. Morita, Carbonization of polyimide film "Kapton", Carbon 27 (1989) 253–257.

[62] Q. Du, T. Chen, J. Liu, X. Zeng, Surface microstructure and chemistry of polyimide by single pulse ablation of picosecond laser, Appl. Surf. Sci. 434 (2018) 588–595.

[63] K.C. Yung, D. Zeng, T.M. Yue, XPS investigation of Upilex-S polyimide ablated by 355 nm Nd: YAG laser irradiation, Appl. Surf. Sci. 173 (2001) 193–202.

[64] T. Jiao, H. Zhao, J. Zhou, Q. Zhang, X. Luo, J. Hu, Q. Peng, X. Yan, Self-assembly reduced graphene oxide nanosheet hydrogel fabrication by anchorage of chitosan/silver and its potential efficient application toward dye degradation for wastewater treatments, ACS Sustain. Chem. Eng. 3 (2015) 3130–3139.

[65] M. Kaba, N. Raklaoui, M.-F. Guimon, A. Mas, Improvement of the water selectivity of ULTEM poly (ether imide) pervaporation films by an allylamine-plasma-polymerized layer, J. Appl. Polym. Sci. 97 (2005) 2088–2096.

[66] M.C. Burrell, J.J. Chera, Polyetherimide (Ultem®) spin cast films by XPS, Surf. Sci. Spectra 6 (1999) 18–22.

[67] H. Estrade-Szwarckopf, XPS photoemission in carbonaceous materials: a "defect" peak beside the graphitic asymmetric peak, Carbon 42 (2004) 1713–1721.

[68] Q. Yuan, C.-T. Lin, K.W. Chee, All-carbon devices based on sp2-on-sp3 configuration, APL Mater. 7 (2019), 030901.

[69] M.C. Biesinger, Accessing the robustness of adventitious carbon for charge referencing (correction) purposes in XPS analysis: insights from a multi-user facility data review, Appl. Surf. Sci. 597 (2022), 153681.

[70] B.-K. Chen, C.-T. Su, M.-C. Tseng, S.-Y. Tsay, Preparation of polyetherimide nanocomposites with improved thermal, mechanical and dielectric properties, Polym. Bull. 57 (2006) 671–681.

[71] M. Yilmaz, N.F. Yilmaz, M.F. Kalkan, Rheology, crystallinity, and mechanical investigation of interlayer adhesion strength by thermal annealing of polyetherimide (PEI/ULTEM 1010) parts produced by 3D printing, J. Mater. Eng. Perform. 1–10 (2022).

[72] P. Huang, Y. Zhao, S. Kuga, M. Wu, Y. Huang, A versatile method for producing functionalized cellulose nanofibers and their application, Nanoscale 8 (2016) 3753–3759.

[73] J.E. Ferl, E.R. Long, Infrared spectroscopic analysis of the effects of simulated space radiation on a polyimide, IEEE Trans. Nucl. Sci. 28 (1981) 4119–4124.

[74] J.-S.-M. Lee, M.E. Briggs, C.-C. Hu, A.I. Cooper, Controlling electric double-layer capacitance and pseudocapacitance in heteroatom-doped carbons derived from hypercrosslinked microporous polymers, Nano Energy 46 (2018) 277–289.